INSTITUTE OF PHYSICS PUBLISHING SUPERCONDUCTOR SCIENCE AND TECHNOLOGY
Supercond. Sci. Technol. **15** (2002) 1436–1444 PII: S0953-2048(02)37318-4

Sinter-forging of strongly textured Bi2223 discs with large J_cs: nucleation and growth of Bi2223 from Bi2212 crystallites

E Guilmeau, D Chateigner and J G Noudem

CRISMAT Laboratory, 6 Bd Marechal Juin, 14050 CAEN, France

E-mail: emmanuel.guilmeau@ismra.fr

Received 22 May 2002, in final form 23 August 2002
Published 20 September 2002
Online at stacks.iop.org/SUST/15/1436

Abstract
Dense Bi2223 superconductor discs with a highly oriented structure were prepared by the sinter-forging method. A detailed investigation of the processing parameters has been carried out on the phase assemblage, the particle size of the calcined precursor powder and the sinter-forging time and temperature. A high transport critical current density, J_c, was obtained from a starting powder rich in Bi2212 and secondary phases. Using fine powder, a high degree of orientation, larger than those of multifilamentary tapes, and excellent intergrain connection were observed. The optimal sinter-forging temperature was found to be in the range of 845–850 °C and the transport critical current densities reached values of 12 700 A cm^{-2} at 77 K in self-field. The combination of textural and microstructural investigations testify that a nucleation-growth mechanism from the Bi2212 particles is responsible for the Bi2223 phase formation, rather than an intercalation process.

1. Introduction

Dense (Bi, Pb)$_2$Sr$_2$Ca$_2$Cu$_3$O$_{10+x}$ ceramics textured by sinter-forging exhibit among the best superconducting properties for bulk superconductors, with critical current densities of about 10 000 A cm^{-2} at 77 K in a self magnetic field. However, transport properties obtained by several authors [1–3] remained stagnant. The composition of the starting powder is probably the main cause of such saturation. To our knowledge, sinter-forging techniques have always used pellets composed of highly pure Bi2223 powder. Chen *et al* [4] stated that the aim of their work was to develop a process for the industrial production of superconductors in which they hoped to avoid a final annealing step. The typical sinter-forging method, which uses a highly pure Bi2223 powder, requires a precise control of the temperature to allow a weak partial fusion of the Bi2223 phase in order to produce enough liquid phase to allow sufficient grain sliding. This weak decomposition is difficult to control and generally leads to a decrease of the Bi2223 phase content.

An alternative route for the formation of Bi2223 would be to start the reactions from calcined powders composed of Bi2212 and secondary phases such as Ca$_2$PbO$_4$, CaCuO$_3$ or CuO [5–9]. This would allow the plate-like grains to reorient more easily because of the large amount of liquid phase. Consequently, improved grain connectivity, through grain alignment, can be expected compared to other typical sinter-forging methods. The calcination-sinter-forging method (CSF) can be compared to the powder-in-tube (PIT) technique with the exception that in PIT, the Bi2223 phase is formed during the sintering steps in a classical furnace. This is notably confirmed by several PIT studies. For example, Yamada *et al* [10] demonstrated that the critical current density was low when the precursor powder was composed mostly of the Bi2223 phase. Hence, one can expect a significant improvement in the transport properties of the bulk samples by modifying the precursor powder phase assemblage. Furthermore, one of the keys to prepare samples which exhibit high critical current densities (J_c) is to control the grain size. Many groups reported that with the PIT process, a small grain size is favourable to obtain a high J_c [11–14]. A fine precursor powder increases the reactivity, which under appropriate conditions promotes the Bi2223 phase formation and increases the intergrain connectivity.

However, the effect of grain size on the superconducting properties of the materials obtained by the CSF process is

 © 2002 IOP Publishing Ltd Printed in the UK

not known. The aim of the present study is to address this question in the case of discs textured by the CSF process and to determine the best sinter-forging conditions with a view to improve the transport critical current densities and the quality of the superconducting transition, as seen by the sharpness of the susceptibility curves. The growth mechanisms involved in the Bi2223 phase formation using this process are discussed.

2. Experimental details

Powders were prepared by the EDTA sol-gel method [15] using the nominal composition $Bi_{1.85}Pb_{0.35}Sr_2Ca_2Cu_{3.1}O_{10+\delta}$. The resulting powder was then calcined under air at 820 °C for 24 h [16, 17] and ground in an agate mortar. The powder was sieved at different sizes (63, 100, 200 μm), hereafter referred to as powders P63, P100 and P200, respectively.

The particle size distribution of powders was analysed by a Mastersizer Malvern analyser. In order to disperse the agglomerates, the powders were subjected to ultrasonic agitation in alcohol prior to their insertion into the sample cell.

The well-established sinter-forging method was used to fabricate superconducting discs. The powders were cold-pressed into 2 mm thick and 25 mm diameter pellets, under uniaxial pressure of 23 MPa, which resulted in a green density of 60% of the theoretical value. The pellets were then placed in the furnace [18] between two 0.125 mm silver sheets to avoid reaction with the alumina supports during heating. The pressure employed during heating was fixed at 10 MPa and the operating temperature ranged between 838 °C and 855 °C. The temperature should be sufficiently high to limit the Bi2223 decomposition which occurs below 822 °C under air at ambient pressure. The furnace was turned off immediately after the pressure was released in order to fix the equilibrium phases and to avoid any decomposition into the secondary phases at low temperature.

Discs D63, D100 and D200 were then sinter-forged at 838 °C for 20 h from precursors P63, P100 and P200, respectively. For the pellets made of P63, sinter-forging was also performed at 838 °C, 845 °C and 850 °C, each for three different durations of 20, 50 and 100 h. From sample mass and volume determination, the density values of our samples is near 90%, compared to the theoretical value of 6.2 g cm^{-3}. Discs were cut into sticks and annealed under 7.5% O_2 and 92.5% N_2 at 820 °C for 100 h, cooled at 1 °C h^{-1} to 800 °C and then quenched to room temperature.

XRD measurements were performed on a 4-circle X'PERT Philips goniometer in the Bragg–Brentano geometry. The incident plane of the x-rays was positioned parallel to the cylinder axis of the samples. A first azimuthal scan (φ-scan) was operated on the (119) reflection in order to check for specific texture symmetries. As expected for uniaxially deformed materials without subsequent growth, we detected a C_∞ axis of symmetry aligned with the cylinder axis, as reported by other authors [19]. Then, tilt scans (ψ-scans) were performed from $\psi = 0°$ to $\psi = 85°$ in steps of 5°. However, in such materials the presence of several low crystal-symmetry phases makes the texture analysis a complex problem, when working with a point detector. Strong peak overlaps occur which do not guarantee that the signal observed by the point detector is actually composed of one reflection or several, and from a single phase or not. This is particularly true at high ψ values for which high beam defocusing arises. One way to overcome this problem is to use a position sensitive detector (PSD) and treat the diagrams in order to deconvolute the different signals from the different phases [20]. In our case, since no PSD was available, we decided to measure θ–2θ scans from 21.5° to 25.5° (width = 0.02°) in order to encompass the 008 and 00$\underline{10}$ reflections of Bi2212 and Bi2223, respectively. The two contributions were deconvoluted by fitting the x-ray profiles using a pseudo-Voigt peak shape, for each ψ position of the sample. A 0.5 mm × 0.5 mm collimated beam and a small vibration of the sample holder (1 mm) were used in order to ensure that the beam remained focused on the sample in the analysed 2θ range (even at high sample tilts) and that the number of irradiated crystallites was statistically relevant (more than 30 000 grains were probed under these conditions). The integrated areas from these scans were used as input to reconstruct ψ-scans which represent the $\{00l\}$ plane dispersions of the crystallites. These were then fitted as Gaussian orientation distributions and normalized into distribution densities by direct normalization procedure [21]. The full width at half maximum of the distribution densities (FWHDs) was used as a quantitative appreciation of the crystallite dispersion. For distribution densities, the m.r.d. (multiple of a random distribution) unit is used. A perfectly non-oriented powder exhibits 1 m.r.d. values for all ψs (its ψ-scan is a straight line) while a textured sample exhibits minima and maxima of densities.

The volume percentage of Bi2223 and Bi2212 phases was calculated on the basis of the corresponding {00$\underline{10}$} and {008} pole figures, obtained from the distribution density scans. However, a problem exists. From only classical θ–2θ scans, one cannot accurately estimate the phase contents of textured materials, since diffracted intensities are affected by the texture itself, which is *a priori* unknown for all phases. Furthermore, the texture of the different phases may be different. Thus, we integrated the measured and normalized pole figures in order to sum the reflection contributions over the sample orientations. The volume percentage was then calculated from these integrated intensities and the structure factors of the corresponding lines.

The transport critical current densities $\left(J_{c_T}\right)$ of our samples (10 × 2 × 0.2 mm^3) were characterized by the standard four-probe technique at 77 K with an electric field criterion of 1 μV cm^{-1}. The magnetization was measured using a SQUID magnetometer. The dimensions of the samples were approximately 4 × 1.5 × 0.2 mm^3. Microstructures of the powder were analysed with a scanning electron microscope (SEM) Philips XL 30 FEG.

3. Results

3.1. CSF process and precursor particle sizes

In order to explain the beneficial effects of the CSF process, the role of particle size on the phase formation and transport properties was examined. The choice of appropriate precursor powder seems to be essential to obtain strongly textured samples.

The 820 °C/24 h calcination leads to a powder composed principally of Bi2212, Ca_2PbO_4, CuO, $Sr_{14}Cu_{24}O_{41}$, Ca_2CuO_3

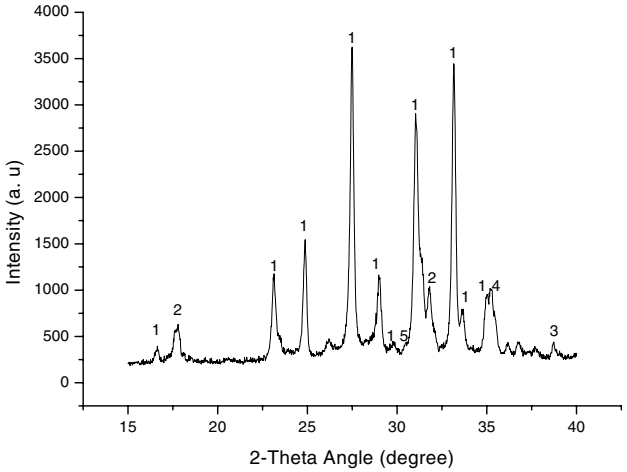

Figure 1. XRD pattern of calcined powder P63 (820 °C/24 h) showing the presence of the (1) Bi2212, (2) Ca_2PbO_4, (3) CuO, (4) Ca_2CuO_3 and (5) $Sr_{14}Cu_{24}O_{41}$ phases.

Table 1. Average size of particles for powders (a) P63, (b) P100 and (c) P200.

Sieve size (μm)	63	100	200
Average particle size (90%) (μm)	8.74	10.18	36.83

and $CuSrO_2$. The three precursor powders (P63, P100 and P200) exhibit similar XRD patterns, with the Bi2212 phase being predominant, as illustrated in figure 1 for the powder P63. The particle size distributions of the powders are shown in figure 2 and the average particle sizes are listed in table 1. As expected, sieving with larger sieve sizes results in a larger average precursor particle size, 50% of the total volume containing particles smaller than 3 μm in P63 and P100 for only 30% in P200. The powders exhibit bi- or trimodal size distributions centred around 0.5 μm, 3 μm and 20–30 μm, the last mode appearing at the expense of the two former ones. Numerous large agglomerates (>30 μm) are present in the powders sieved at 100 and 200 μm, while using a 63 μm sieve severely limits their number. Such agglomerates consist of Bi2212 platelets with small particles of secondary phases on their surface, as shown in figure 3. These agglomerates, formed during calcination, were not completely dispersed by ultrasonic agitation which implies the presence of a strong intra-agglomerate grain connectivity. In such conglomerates, sliding of Bi2212 platelets under uniaxial pressure becomes more difficult than that for individual particles. Furthermore, the large agglomerates are poorly connected to each other and may limit both the contacts between Bi2212 and the secondary phases and the diffusion paths.

Figure 4 shows a typical XRD pattern of the textured samples D63, D100 and D200, in which Bi2212 is the dominant phase. Phases related to the Sr–Ca–Cu–O system are also observed. From such diagrams, the average diffraction-coherent domain size (crystallites) was calculated using the Scherrer formula and 00*l* lines to be around 60 nm, a value similar to observations of other groups, without significant differences between the samples.

Figure 5 shows a typical SEM cross-section of the samples where the aligned platelet grains and unconsumed secondary phases can be observed. At this magnification, it is difficult to evaluate the FWHDs (presented below), particularly within a resolution of a few tenths of degrees which can considerably influence the superconducting properties.

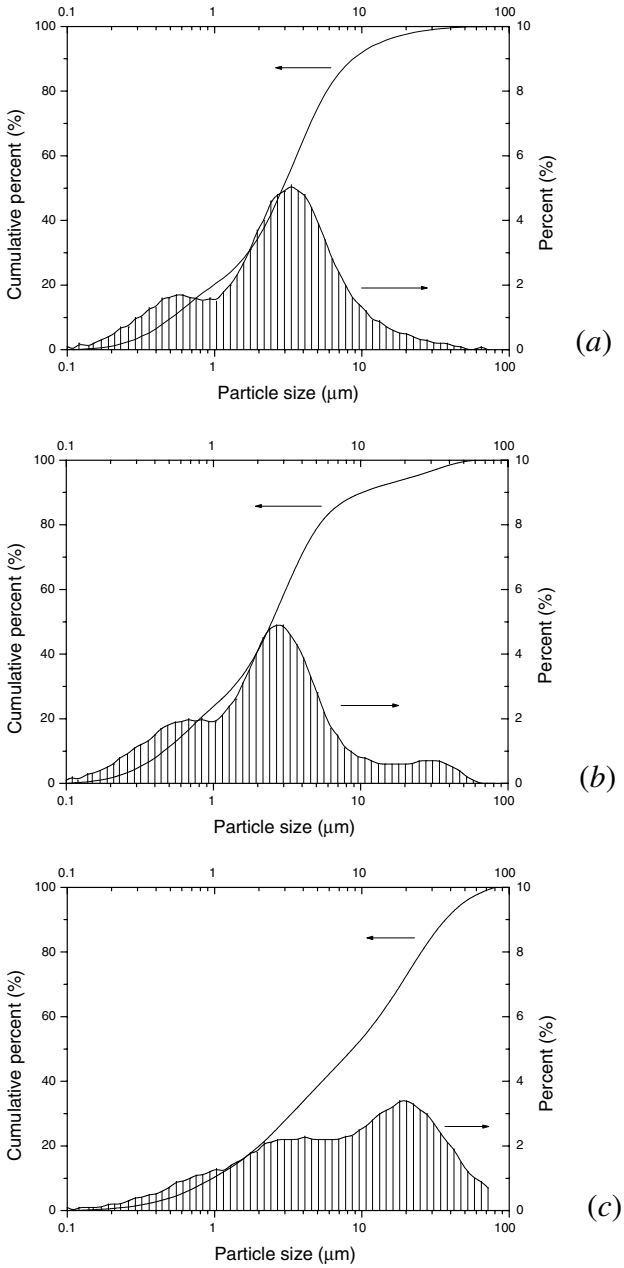

Figure 2. Particle size distributions of powders P63 (*a*), P100 (*b*) and P200 (*c*).

3.2. Texture stabilization of Bi2212 and Bi2223

Figure 6(*a*) shows the {008} and {00$\underline{10}$} normalized pole figures of the Bi2212 and Bi2223 phases of sample D63, respectively. The *c*-axes distributions of the two phases are very similar with only 5 m.r.d. of difference at the maximum of the distribution. However, this slight difference may be important in the evaluation of the phase content. For both phases the minimum distribution density observed is 0 (figure 6(*b*)), for angles as low as $\psi \approx 27^\circ$, while the value for a powder (1 m.r.d.) is achieved at $\psi \approx 25^\circ$.

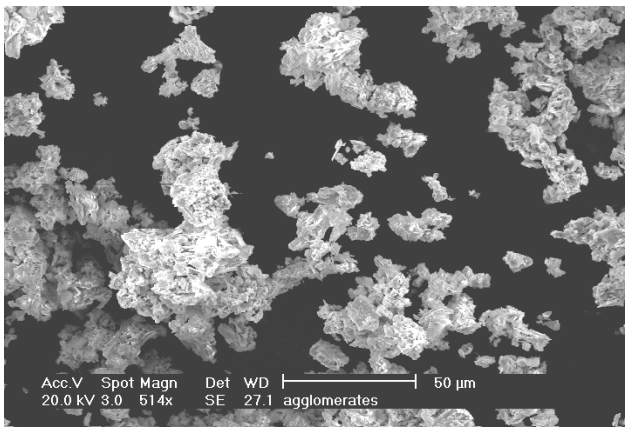

Figure 3. SEM image of P200 calcined powder showing the presence of large agglomerates.

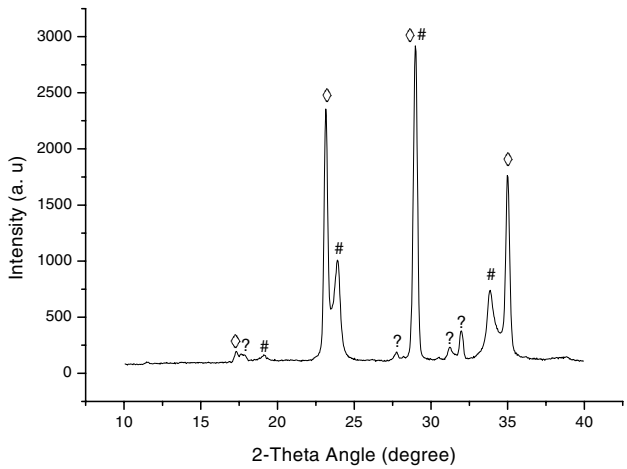

Figure 4. X-ray diffraction pattern of synthesized discs. Main (00*l*) peaks of the Bi2212 (◊) and Bi2223 (#) phases are indicated. (?) indicate phases related to Sr–Ca–Cu–O system.

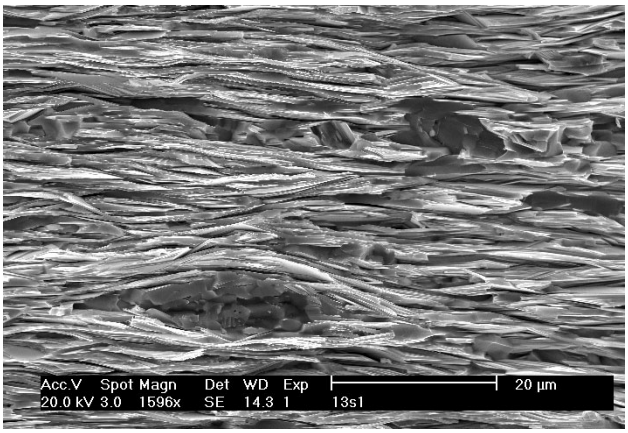

Figure 5. Typical SEM cross-section of samples showing aligned platelet grains and unconsumed secondary phases.

The FWHDs are 16.07° and 15.8° for the Bi2212 and Bi2223 phases, respectively. These values reveal the strong textures achieved by the CSF process and are much stronger than those observed for self-supporting films of clay minerals [22] or of multifilamentary tapes of similar phases [19]. The orientation distributions slightly differ from pure Gaussians, but not significantly, indicating that the interactions which govern the orientation process are not fully represented by a normal statistical law using the CSF process. Since the particle size distributions of our samples are not monomodal, the uniaxial pressure effect may act differently upon different particle sizes, and we attribute this effect to inhomogeneous pressure fields.

3.3. Texture and transport J_c

In figure 7, the FWHDs of the Bi2212 and Bi2223 phases are compared to the critical current density versus the sieve size. The critical current density decreases from 7000 A cm^{-2} for D63 to 4000 A cm^{-2} for D200.

From this figure, it becomes evident that larger particles induce worse grain alignments of both phases, particularly when these particles are composed of many smaller, randomly oriented grains and poor connectivity, which explains the weak transport critical current density of sample D200. The Bi2212 plate-like grains present in the agglomerates move with difficulty and lead to more dispersed textures characterized by lower critical current densities. Furthermore, the large agglomerates result in the existence of large residual phases which hinder somehow the grain alignment of the Bi2223 grains in the matrices and act as barriers for the current paths. The resulting transport properties are, of course, deteriorated.

The difference in FWHDs observed between the two major phases also increases with the sieve size, with the FWHD of Bi2223 constantly smaller than that of Bi2212. This is a strong indication for the initial nucleation of Bi2223 on Bi2212 particles, followed by the naturally faster and more anisotropic growth of Bi2223 crystals. When only small and well-oriented Bi2212 particles exist, they all independently serve as nucleation sites for Bi2223, and the Bi2212 and Bi2223 phases exhibit identical FWHDs. In contrast, in the presence of large agglomerates, Bi2223 nucleates on the Bi2212 crystallites, both on the surface and inside the agglomerates. In both cases, Bi2223 crystallites are able to grow and rotate under the uniaxial pressure as they develop, thereby gaining in texture strength, but with a less degree when Bi2223 forms from the misaligned Bi2212 crystals on the inside of the agglomerates.

To summarize, mean grain size of the precursors affects the transport properties of discs textured by the sinter-forging process, the decrease of J_c with the sieve size being explained both by an increase of the crystallite orientation distribution and by a decrease of grain connectivity.

3.4. J_{c_T} and phase transformation dynamics

The second part of this work focuses on the effects of the CSF process on the phase transformation and superconducting properties. It is important to note that this process is interesting in view of practical applications. Contrary to the classical sinter-forging method [1, 3], CSF omits several sintering steps and intermediate grindings. Intermediate grindings are necessary to accelerate the Bi2223 phase formation in order to obtain a highly pure Bi2223 powder. The retrograde densification of the pellets used for the sintering produces less diffusion paths and a decrease in the Bi2223 kinetics of formation. This retrograde densification can

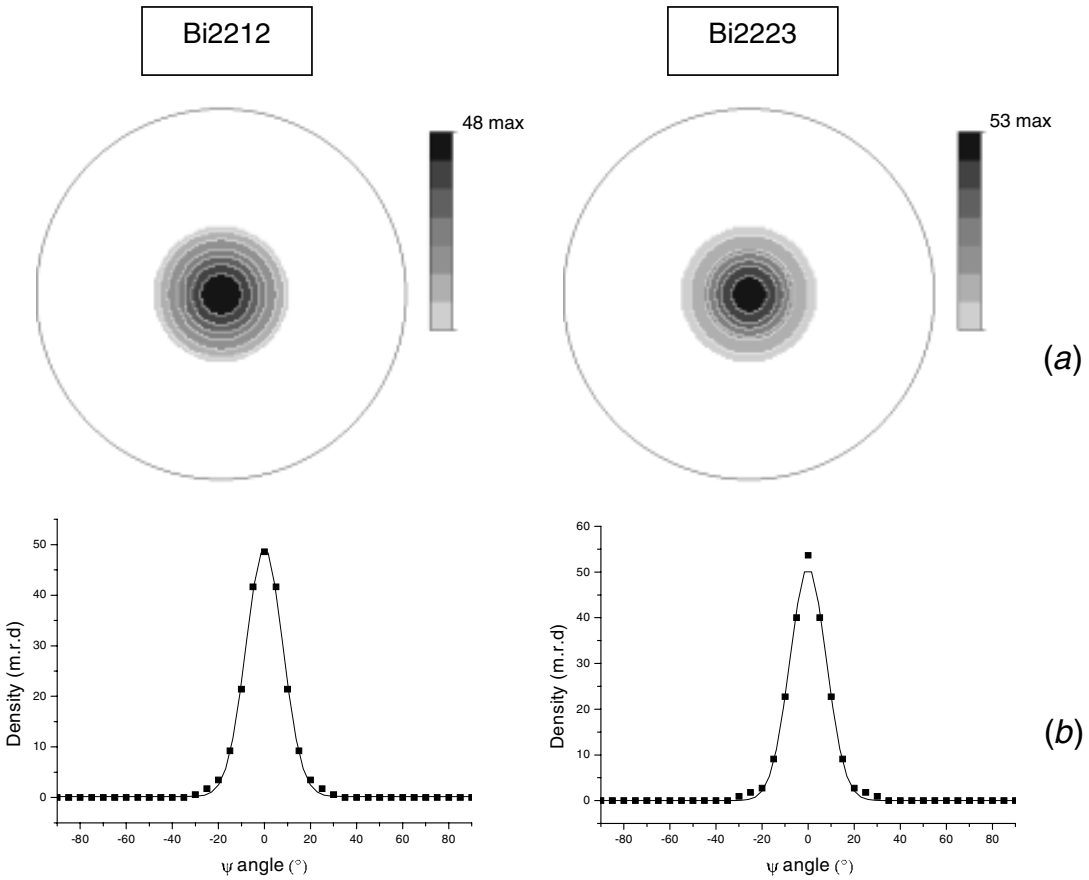

Figure 6. (*a*) {008} (left) and {00$\underline{10}$} (right) normalized pole figures of the Bi2212 and Bi2223 phases, respectively, for sample D63 (equal area projection, linear density scale). Disc axes are centres of pole figures. (*b*) Corresponding ψ-scans (cross-sections of the pole figures) showing the Gaussian fits of the *c*-axis distribution densities.

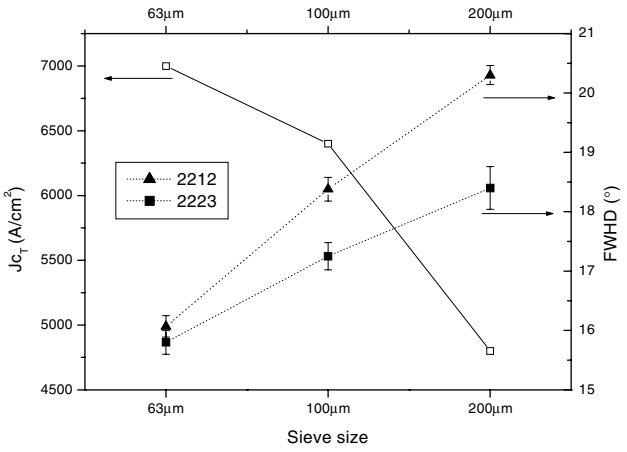

Figure 7. Comparison of transport critical current density and FWHD with sieve size of discs D63, D100 and D200. Sample forged at 838 °C for 20 h.

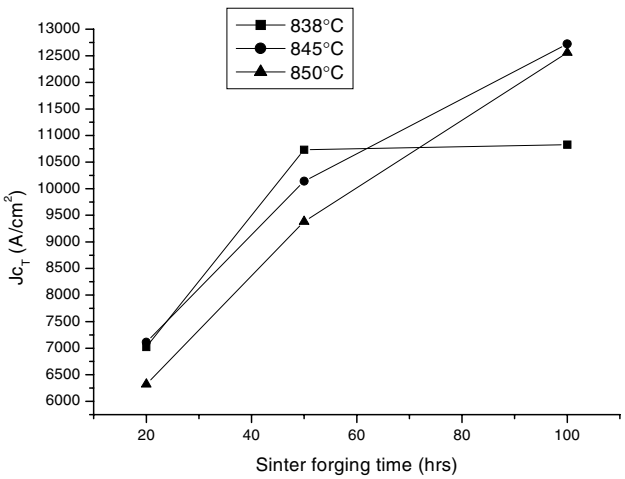

Figure 8. Influence of sinter-forging time on J_{c_T} for discs textured at 838, 845 and 850 °C.

be eliminated by an intermediate grinding. It allows the homogenization of Bi2223 and secondary phase distribution, increasing the specific surface of Bi2223 grains and reducing diffusion path lengths. However, these imposed intermediate grindings and the long sintering steps are restrictive for industrial applications. Hence, the CSF process seems to be more appropriate.

The transport critical current density versus sinter-forging time curves for different sinter-forging temperatures are plotted in figure 8. Temperatures above 850 °C lead to the decomposition of Bi2223 due to the production of excess liquid phase. The transport J_c increases with the sinter-forging time to reach a value of 12 700 A cm^{-2}, much larger than the J_c obtained by the classical sinter-forging process.

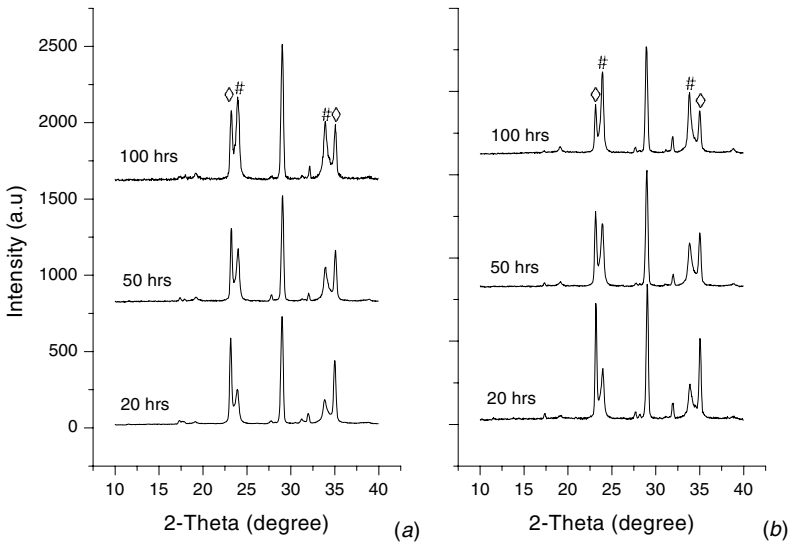

Figure 9. X-ray diffraction patterns of discs sintered at (*a*) 838 °C and (*b*) 845 °C for 20, 50 and 100 h. Main (00λ) peaks of the Bi2212 (◊) and Bi2223 (#) phases are indicated.

The critical current density versus sintering temperature shows that the J_c saturates after 50 h for the discs sintered at 838 °C and continues to increase for temperatures equal to 845 °C and 850 °C. The XRD patterns of discs textured for 20, 50 and 100 h at 838 °C and 845 °C are plotted in figure 9. The XRD patterns of samples textured at 850 °C are similar to those textured at 845 °C and are not shown. Considering that the texture is similar for both phases (which is not strictly true from the previous paragraph), the ratio of Bi2223 increases with sintering time for both samples. However, it is observed that the Bi2223 phase at $T = 838$ °C (figure 9(*a*)) continues to grow more slowly than that corresponding to 845 °C (figure 9(*b*)). By using the x-ray integration method as mentioned earlier, the percentages of Bi2223 can be quantitatively estimated to be about 29.2% and 47.5% for samples textured, respectively, at 838 and 845 °C for 100 h, whereas these ratios are nearly equal to 22% after a 50 h sintering step. Therefore, the stabilization of J_{cT} for the sample elaborated at 838 °C can be explained by a saturation in Bi2223 content. Such a behaviour is explained by phase stability concepts. It has effectively been proved in a previous work [17] that sintering of pellets at 838 °C for 100 h leads to a lower Bi2223 content than in samples sintered at higher temperatures. Furthermore, the smaller quantity of Bi2223 phase in the sample textured at 838 °C can also be explained by a lack of a liquid phase. The liquid phase promotes Bi2223 phase formation and increases grain alignment and connectivity. The formation of the liquid phase during the heat treatment depends on the sintering temperature, the composition, the phase assemblage and the particle size distribution of the precursor powder [14, 23]. At lower temperatures (838 °C), liquid phase promotion is not sufficient to enhance the Bi2223 phase growth which leads to a saturation of the Bi2223 phase formation.

3.5. Texture versus sinter-forging time and phase content

The crystallite distributions of the Bi2212 and the Bi2223 phases and the Bi2223 content of discs textured at 845 °C for 20, 50 and 100 h are shown in figure 10. The FWHD of

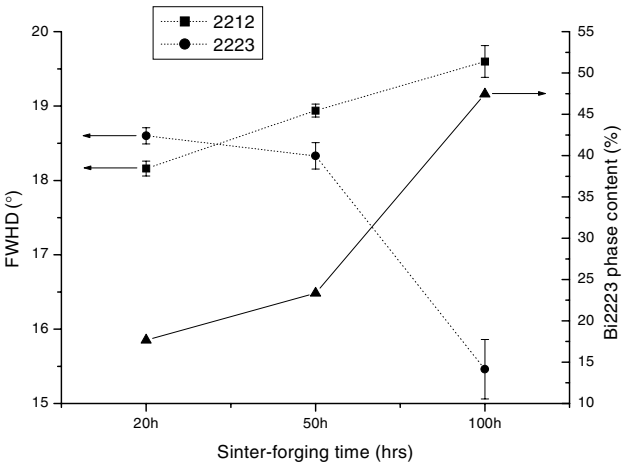

Figure 10. Evolution of Bi2223 phase content and FWHDs with the sinter-forging time for samples textured at 845 °C using a 63 μm sieve size.

the Bi2212 phase increases with the increasing sinter-forging time, while the FWHD of the Bi2223 phase decreases. In the same way, the Bi2223 phase content increases with increasing sinter-forging time. A strong inverse correlation between the FWHD decrease of Bi2223 and the formation of this phase is observed, which is synonymous with a strong growth anisotropy leading to a favourable orientation of crystallites. After nucleation, the growth stage of Bi2223 is responsible for the texture stabilization. Simultaneously, we note a small FWHD increase of the Bi2212 phase. This seems to indicate that the Bi2223 formation and growth is associated with a weak perturbation in the orientation of Bi2212, which is yet to be explained. However, an intercalation process for the Bi2223 phase formation would have retained the initial orientations of Bi2212, and FWHDs of both phases would have evolved contiguously. Our results show that the intercalation process is probably not the major growth scheme, even if it occurs.

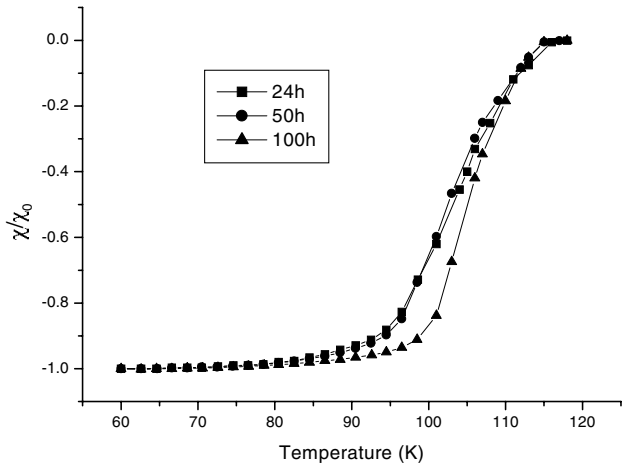

Figure 11. Magnetic susceptibility versus temperature curves of samples textured at 845 °C for different sintering times.

3.6. Magnetic susceptibility versus sintering time

Figure 11 shows the susceptibility curves for different sintering times. The T_c^{onset} of the three samples is not affected. However, a longer sinter-forging treatment leads to a narrower transition, particularly after 50 h of forging. Comparing figures 10 and 11, this observation is consistent with extrinsic contributions such as grain alignment and/or the disappearance of secondary grain interface phases, resulting in better connectivity in the samples textured during 100 h at 845 °C.

4. Discussion

The above results are in contrast with those described by Gottschalck Andersen *et al* [24] and Frello *et al* [25]. The previous authors effectively showed that, independent of the atmosphere, the Bi2223 texture development closely follows that of Bi2212. Their average *c*-axis misalignment angle, $\Delta\alpha$ (defined in [26]), is coherent with the FWHD definition described here. However, for a fixed ω position of their sample, the authors cannot ensure they simultaneously measure the maximum of the distribution for both superconducting phases, although this is partly compensated by the use of a high energy beam. Consequently, comparing $\Delta\alpha$ for the two phases can lead to artefacts. The authors would have needed several two-dimensional patterns measured at different ω angles to correct for this. They observe that the $\Delta\alpha$ of the Bi2223 phase is lower than that of Bi2212 in the first hours of annealing, whereas at the end of the heat treatment, the $\Delta\alpha$ widths of the two phases become identical. Similar results were demonstrated in an *in situ* neutron diffraction study on a multifilamentary tape under 8% O_2 by Fahr *et al* [27]. They found, as had many authors [28, 29], that initially the Bi2223 grains form near the silver interface where they form colonies of well-aligned grains. By increasing the annealing time, Bi2223 grains in the core of the filament appear which are characterized by an inferior degree of alignment. In the CSF process there also exists an interface with Ag foils, but it is restricted at the surface with pistons to avoid interdiffusion of the piston metal and the Bi compounds. Hence, due to the thickness of compounds (0.2–0.3 mm), we do not expect any large influence of the foil on the resulting growing properties, except as a beneficial pressure homogenization due to its larger ductile character. But we systematically observe smaller FWHDs compared to mono- or multifilamentary tapes [19, 24, 26], which could be interpreted as the effect of the mechanical interaction between Ag and Bi2212 or Bi2223 in Ag-sheathed ribbons. In the CSF process no lateral constraint is applied to the cylindrical powders, which allows the discs to laterally extend and thereby promotes a stronger texturation. This is also coherent with the observation that wider tapes [19] with lower side compression exhibit stronger textures than narrower ones [24].

Li *et al* [30] observed a different trend, using the Lotgering [31] x-ray approach to measure the orientation degree of *c*-axes. The Lotgering factor varies from 0 for an entirely non-oriented specimen to 1 for a completely oriented specimen. Since this factor is derived from an average value, it is only possible to compare texture strengths for textures of the same type (specific $\langle hkl \rangle$ fibres, planar, three-dimensional, ...) and has severe limits. For instance, when only 00*l* peaks are observed, the Lotgering factor takes the value 1. But many different textures can be stabilized exhibiting only 00*l* peaks in a given 2θ range, with various dispersions. The correlation between the Lotgering factor and a quantitative description of the texture is then, if at all it exists, subject to caution. Furthermore, the phase content estimate of the authors relies only on the (008)-Bi2212 and (00$\underline{10}$)-Bi2223 peaks of a single θ–2θ diagram, which is correct only for non-oriented powders or for phases having the same texture, which is not the actual case. Consequently, the authors showed that, for a sample composed of a mixture of Bi2223 and Bi2212, the Lotgering factor calculated for the Bi2212 phase increases with increasing mechanical deformation, while the Lotgering factor of Bi2223 decreases with the deformation. This result disagrees with others established for similar powder-in-tube samples [24, 25] and our own results on the correlation of the texture evolutions of Bi2223 and Bi2212 crystallites. We strongly believe that the Lotgering factor approach is not appropriate for the orientation characterization of such samples.

But the treatment employed may also affect the texture and the alignment behaviour. In our case, temperature and uniaxial pressure are combined and induce a continuous deformation and phase transformation. This point is important in the interpretation of results. First, it must be noted that the platelet slide mode in this process is fundamentally different from that in annealing or cold deformation (rolling, pressing, ...). The presence of a liquid phase at high temperature allows smoother sliding and stacking of the platelet grains. In this way, the texture evolution of the Bi2223 and Bi2212 phases may be radically different from those described previously. But this evolution can also be modified by the presence of Ag foils or sheaths. In order to avoid this latter possible effect, we removed the silver foils in our samples before diffraction analysis, which differs from studies of Gottschalck Andersen *et al* and Frello *et al* [24, 25]. In this case, we can suppose that the high oriented texture of the Bi2223 phase on the disc surface, if it exists, has been removed, which is crucial to understanding the Bi2212 to Bi2223 growth mechanisms independent of any other Ag-related

interactions. Furthermore, the thickness of our samples limits the strong influence of the surface texture on the whole sample. With all these precautions, the observation of very similar FWHD values for the Bi2212 and Bi2223 phases at a quasi starting reaction state (i.e. after 20 h of sinter-forging only) for 63 μm size precursors (figure 7) is a strong indication of Bi2223 nucleation on pre-existing Bi2212 crystallites, thereby inheriting the Bi2212 texture at an early stage of the transformation process.

However, the question concerning the different evolution trends of the Bi2212 and Bi2223 FWHD values versus the sinter-forging time (figure 10) remains open. To explain such a behaviour, it is necessary to understand the formation mechanism and the development of the Bi2223 grain texture from Bi2212. Several investigations can be found in the literature which explain the transformation from Bi2212 to Bi2223. They relate two principal possible mechanisms, namely 'the solid-state transformation' or 'intercalation process' and the 'dissolution/crystallization mechanism' or 'nucleation-growth mechanism'. The solid-state transformation occurs within the parent phase and implies elemental diffusion to and/or from the reaction front. The most plausible diffusion channel for this mechanism appears to be a transition region along the *a–b* planes. In this case, the intercalation front proceeding in the Bi2212 phase implies a texture distribution (FWHD) equal for the two Bi2212 and Bi2223 phases. The nucleation-growth mechanism consists of dissolution of the parent phase and nucleation and growth of the second phase, either as separate or epitaxially-related grains. Contrary to the solid-state transformation, Bi2212 plays the role of a substrate and the Bi2223 phase grows on the parent phase. The effect of annealing induces the growth of the Bi2223 phase which consumes the Bi2212 phase, and the *c*-axis of the Bi2223 grains aligns to a certain degree to the disc normal.

Such a mechanism seems to be well suited to explain our results. In the first hours of sinter-forging, the Bi2212 platelet grains flow rapidly, thanks to the presence of a large quantity of liquid phase. Thus, the first crystallites of Bi2223 inherit the Bi2212 texture and present the same FWHD value after a 20 h sinter-forging. By increasing the annealing time, the Bi2223 grains grow and improve the grain alignment due to their larger anisotropic intrinsic growth. At the same time, Bi2212 is consumed and displays increasingly less texture cohesion in the whole sample. This behaviour results in an increase of the FWHD of Bi2212 and a large decrease of the FWHD of Bi2223.

Although the texture evolution observed by Gottschalck Andersen *et al* [24] and Frello *et al* [25] is contrary to our results, the conclusions, in terms of transformation mechanism, are similar and show that the transformation mechanism is probably a nucleation-growth model with the decomposition of Bi2212 and the growth of the Bi2223 phase.

It is also important to note that, even after 100 h, the grain alignment and the Bi2223 content continue to improve. The uniaxial pressure applied to shape the pellets allows for the compaction by reorientation of the different phases, and eventually crystallite cleavages occur. Yau *et al* [32] related a smaller stacking fault energy of the basal plane of Bi2223 relative to Bi2212, in strongly deformed multifilament Ag-sheathed tapes. At the late stages of our CSF process, when less liquid is present, cleavage may occur as a minor orientation process. The solid-state reorientation by cleavage and rotation of the Bi2223 crystallites is also coherent, as observed in this work, with a more pronounced orientation of the Bi2223 crystallites relative to Bi2212 due to a lower stacking fault energy of the former phase. But the most likely process activated to explain the orientation phenomenon is still rotation of solid particles in a partially liquid state.

The Bi2223 phase is easily formed using the CSF process because the high compaction of the material in the pressure direction is not limited by transversal forces, giving rise to a larger number of contacts between Bi2212 platelets and secondary phases. Platelet sliding or reorientation induced by the uniaxial pressure during the heat treatment improves the density and connects the plate-like grains. The Bi2223 phase continues to form while the grain flow favours liquid phase incorporation in the cavities. It is therefore important to work at a temperature sufficiently high to produce an appropriate amount of liquid phase using the CSF process. However, the liquid phase needs to be consumed in order to form the Bi2223 phase and to avoid the presence of large secondary phases in the discs after sinter-forging, phases which hinder the grain connectivity and the current transport.

The CSF process has proved to be an effective method to texture Bi2223 compounds. However, the characteristics of the best samples are still not optimized. The Bi2223 phase content is relatively weak and must be increased in order to improve critical current density. Also, the texture improvement using this method proves that J_{c_T} gains are still attainable by achieving stronger crystallite alignments. To these ends, an additional study based on the effects of precursor powder grinding on the Bi2223 phase formation and superconducting properties is currently under investigation. An improvement of the powder reactivity would be effective to obtain discs with high Bi2223 phase content and better grain alignment.

5. Conclusion

Sinter-forging of a precursor powder composed of Bi2212 and secondary phases has been used to increase the formation of Bi2223 phase content. Highly dense and textured discs with the *c*-axis of the constituting grains parallel to the direction of the applied stress have been synthesized. The critical current density obtained by the new CSF process is much larger than that obtained by the typical sinter-forging method, reaching values of 12 700 A cm^{-2} in self-field at 77 K on bars cut from the textured samples. To our knowledge, the texture levels reached in the samples are higher than those in any other published results for this kind of material, with half-widths of dispersions around 16° and strongly decreasing weak links. During hot-forging treatment, the Bi2223 phase formation depends on the grain size, temperature, texture formation and sintering time. The best results are achieved for powders sieved with a 63 μm sieve, temperature between 845 and 850 °C and a time of 100 h. Longer sinter-forging times lead to a sharper magnetic superconducting transition, a higher Bi2223 phase content and a stronger *c*-axes orientation. Further investigations of thicker samples with the same degree of texture and high transport critical current density are underway.

Acknowledgments

E Guilmeau is grateful to the 'French Ministère de la Recherche et de la Technologie' for his PhD fellowship.

References

[1] Rouessac V, Poullain G, Provost J, Gomina M and Desgardin G 1998 *Eur. Phys. J.* **AP2** 145
[2] Tampieri A, Celotti G, Calestani G and Lesca S 1997 *Key Eng. Mater. Euro Ceram. V* **132** 1247
[3] Guilmeau E and Noudem J 2002 *Supercond. Sci. Technol.* at press
[4] Chen N, Biondo A C, Dorris S E, Goretta K C, Lanegan M T, Yougdahl C A and Poeppel R B 1993 *Supercond. Sci. Technol.* **6** 674
[5] Wang M, Xiong G, Tang X and Hong Z 1993 *Physica* C **210** 413
[6] Murashov V A, Ionescu M, Murashova G E, Dou S X, Liu H K and Apperley M 1997 *Inst. Phys. Conf. Ser.* 158 pp 937
[7] Chen F H, Koo H S and Tseng T Y 1991 *Appl. Phys. Lett.* **58** 637
[8] Shi D, Boley M S, Chen J G, Xu M, Vandervoort K, Liao Y X and Zangvil A 1989 *Appl. Phys. Lett.* **55** 699
[9] Uzumaki T, Yamanaka K, Kamehara N and Niwa K 1989 *Japan. J. Appl. Phys.* **1** 75
[10] Yamada Y, Obst B and Flükiger R 1991 *Supercond. Sci. Technol.* **4** 165
[11] Su X-d, Yoo J-m, Ko J-w, Kim H-d, Chung H-s, Yang Z Q and Qiao G-w 2000 *Physica* C **331** 285
[12] Vo N V, Willis J O, Peterson D E, Liu H K and Dou S X 1998 *Physica* C **299** 315
[13] Xia S K, Lisboa M B, Polasek A, Sens M A, Serra E T, Rizzo F and Borges H 2001 *Physica* C **354** 467
[14] Li Q, Brodersen K, Hjuler H A and Freltoft J 1993 *Physica* C **217** 360
[15] Rouessac V, Wang J, Provost J and Desgardin G 1996 *J. Mater. Sci.* **31** 3387
[16] Garnier V, Monot I and Desgardin G 2000 *Supercond. Sci. Technol.* **13** 602
[17] Guilmeau E, Andrzejewski B and Desgardin G *Physica* C at press
[18] Rouessac V, Wang J, Provost J and Desgardin G 1996 *Physica* C **268** 225
[19] Wenk H-R, Chateigner D, Pernet M, Bingert J, Hellstrom E and Ouladdiaf B 1996 *Physica* C **272** 1
[20] Ricote J and Chateigner D 1999 *Boletín de la Sociedad Española de Cerámica y Vidrio* **38** 587
[21] Manceau A, Lanson B, Chateigner D, Wu J, Huo D F, Gates W P and Stucki J W II 2000 Structural chemistry of reduced Garfield nontronite *Am. Mineral.* **85** 153
[22] Manceau A, Chateigner D and Gates W P 1998 *Phys. Chem. Miner.* **25** 347
[23] Jiang J and Abell J S 1998 *Physica* C **296** 13
[24] Andersen L Gottschalck, Poulsen H F, Abrahamsen A B, Jacobsen B A and Tschentscher T 2002 *Supercond. Sci. Technol.* **15** 190
[25] Frello T, Poulsen H F, Andersen L Gottschalck, Andersen N H, Bentzon M D and Schmidberger J 1999 *Supercond. Sci. Technol.* **12** 293
[26] Andersen L Gottschalck 2001 *PhD Thesis* Technical University of Denmark and Risø National Laboratory webpage http://www.risoe.dk/rispubl/AFM/ris-r-1271.htm
[27] Fahr T, Trinks H-P, Schneider R and Fischer C 2000 *Proc. Applied Superconductivity Conf. 2000*
[28] Feng Y, High Y E, Larbalestier D C, Sung Y S and Hellstrom E E 1993 *Appl. Phys. Lett.* **62** 1553
[29] Yamada Y, Xu J Q, Kessler J, Seibt E, Goldacker W, Jahn W and Flükiger R 2000 *Physica* C **185–189** 2483
[30] Li S, Hu Q Y, Liu H K, Dou S X and Gao W 1997 *Physica* C **279** 265
[31] Lotgering F K 1959 *J. Inorg. Nucl. Chem.* **9** 113
[32] Yau J K, Munroe P R and Sorrell C C 1995 *Physica* C **243** 359